KSCE Journal of Civil Engineering (2013) 17(5):1166-1178
DOI 10.1007/s12205-013-0049-y

Water Engineering
www.springer.com/12205

Analysis on Failure of Slope and Landslide Dam

Ram Krishna Regmi*, Giha Lee, and Kwansue Jung*****

Received January 26, 2012/Accepted October 23, 2012

Abstract

A three-dimensional (3D) seepage-flow numerical simulation model was developed for seepage analysis of a landslide dam. A 3D seepage-flow numerical simulation model coupled with a two-dimensional (2D) surface flow and erosion/deposition model was developed for seepage analysis of a slope due to a rainfall event. The conventional water-phase (one-phase) seepage-flow model assumed only water-phase flow in seepage analysis, which was inadequate for unsaturated soil domains. A water-air two-phase seepage-flow model that considers both the water and air phases in the seepage-flow process was also used for the seepage analysis. The pore-water pressure and moisture-content data obtained from the seepage-flow model were used to analyze the stability. Janbu's simplified method and the extended Spencer method were used for the stability analysis. The numerical simulation results almost compared well with laboratory experimental measurements.

Keywords: *unsaturated soil, water-air two-phase flow, numerical simulation, slope stability*

1. Introduction

In general, rainfall-induced slope failures are caused by increased pore pressure and seepage force during periods of intense rainfall. The effective stress in the soil decreases due to the increased pore pressure, reducing the soil shear strength, and ultimately resulting in slope failure. During rainfall, a wetting front moves downward into the slope, resulting in a gradual increase in water content and decrease in negative pore-water pressure. This negative pore-water pressure is referred to as matric suction when referencing the pore-air pressure that contributes to unsaturated soil slope-stability.

Various physical models coupling infinite slope-stability analyses with hydrological modeling have been developed assuming a steady or quasi-steady water table and groundwater flow parallel to the hill slope. Tsai *et al*. (2008) developed a physically model using the complete Richards' equation with the effect of slope angle and also adopted the extended Mohr-Coulomb failure criterion (Fredlund *et al*., 1978) to describe the unsaturated shear strength.

Sassa (1972, 1974) conducted a series of flume tests and concluded that the changes in rigidity of sand and the upper yield strain within a slope were essential to slope-stability analyses. Fukuzono (1987) conducted an experiment to examine the conditions leading to slope failure using near-actual-scale slope models providing heavy rainfall. Crozier (1999) tested a rainfall-based landslide-triggering model developed from landslide episodes in Wellington City, New Zealand, termed the Antecedent Water Status Model, to predict landslide occurrence by providing a 24-hour forecast. Sharma (2006) conducted experimental and numerical studies to investigate the effects of slope angle on moisture movement into unsaturated soil domains and further on the slope-stability, and he also analyzed the difference in failure pattern and moisture movement in single and double layers of soil with different hydraulic conductivities. Tsustumi and Fujita (2008) investigated several landslide sites and used physical experiments and numerical simulations with a combination of rainwater infiltration for their slope-stability analysis. Mukhlisin and Taha (2009) developed a numerical model to estimate the extent of rainwater infiltration into an unsaturated slope, the formation of a saturated zone, and the change in slope stability. Then, the model was used to analyze the effects of soil thickness on the occurrence of slope failure.

Landslide dam failure has been frequently studied as an earthen dam failure despite their differences in geometry, dimensions, and material properties. Numerical models from various literatures allow rough computation of the hydrograph resulting from the dam failure; however, they do not give any indication regarding the whole dam stability. Many researchers, such as Takahashi *et al*. (1994), Mizuyama *et al.* (2006), Davies *et al.* (2007), Satofuka *et al.* (2010) and others proposed numerical models to estimate the outflow hydrograph resulting from the overtopping failure of a landslide dam. Some of them investigated the erosion process associated with the overflow.

*Researcher, International Water Resources Research Institute, Chungnam National University, Daejeon 305-764, Korea (E-mail: rkregmi@engineer.com)
**Assistant Professor, Dept. of Construction & Disaster Prevention Engineering, Kyungpook National University, Sangju 742-711, Korea (Corresponding Author, E-mail: leegiha@knu.ac.kr)
***Member, Professor, Dept. of Civil Engineering, Chungnam National University, Daejeon 305-764, Korea (E-mail: ksjung@cnu.ac.kr)

Very few models have been developed to analyze the stability of a landslide dam. Most of them are applicable for 2D analyses. Takahashi *et al.* (1988) developed a numerical model to predict the hydrograph of debris flow in case of overtopping and sliding, while Awal *et al.* (2008) developed a model that can predict the failure time and failure mode either due to overtopping or due to sliding as well as the resulting water and sediment flow hydrographs. Awal *et al*. (2009) investigated the sudden sliding failure of a landslide dam in three dimensions.

The above-discussed numerical studies related to landslides are applicable only to 2D analyses, whereas slope failure occurs in three dimensions. Although a study of the failure of a landslide dam was also investigated in three dimensions, the stability analysis was carried out using Janbu's simplified method that satisfies only the force equilibrium. However, it is necessary to satisfy all the conditions of equilibrium to get a more accurate result. Furthermore, soil slopes have both water and air phases. Although pore air and water both influence seepage flow, all of the above-mentioned studies neglected airflow in their seepage analyses. In examining the behavior of unsaturated soils, authors such as Dakshanamurthy *et al.* (1984) incorporated the airflow within the soil, proving it to be significant to the overall soil behavior. Therefore, a numerical study in three dimensions is necessary for seepage and slope stability analyses that consider the effects of the air phase in the seepage.

This study analyzed slope failure due to rainfall and the sudden sliding of a landslide dam using the pore-water pressure and moisture content calculated with a conventional water-phase seepage-flow model and a water–air two-phase seepage-flow model. Janbu's simplified method and the extended Spencer method were incorporated into dynamic programming to locate the critical slip surface of a general slope. The simulation results were compared with experimental results to evaluate the model.

2. Numerical Modeling

2.1 Seepage Flow Model

The pressure-based Richards' equation (Eq. (1)), valid for variably saturated soil, was used in a conventional 3D seepage-flow model to calculate the change in pore-water pressure inside the soil domains (Awal *et al*., 2009).

$$(C+S_wS_s)\frac{\partial h_w}{\partial t}=\frac{\partial}{\partial x}\left(K_{wx}\frac{\partial h_w}{\partial x}\right)+\frac{\partial}{\partial y}\left(K_{wy}\frac{\partial h_w}{\partial y}\right)+\frac{\partial}{\partial z}\left(K_{wz}\left(\frac{\partial h_w}{\partial z}+1\right)\right) \tag{1}$$

where h_w is the water pressure head; K_{wx}, K_{wy}, and K_{wz} are the hydraulic conductivity in the x, y, and z directions, respectively; $C=\partial\theta_w/\partial h_w$ is the specific moisture capacity; θ_w is the soil volumetric water content; S_w is the saturation ratio; S_s is the specific storage; t is the time; x and y are the horizontal spatial coordinates; and z is the vertical spatial coordinate taken as positive upwards. S_s depends on the compressibility of the solid matrix and fluid, so it approaches zero in an unsaturated, unconfined porous medium.

To solve Eq. (1), the following constitutive relationships proposed by van Genuchten (1980) were used for establishing the relationship of $\theta_w - h_w$ and $K_w - \theta_w$:

$$S_e=[1+(|\alpha h_w|)^{\eta}]^{-m} \tag{2}$$

$$S_e=\frac{\theta_w-\theta_r}{\theta_s-\theta_r} \tag{3}$$

$$C=\frac{(n-\theta_r)\eta\ m\ \alpha\,|\alpha\ h_w|^{\eta-1}}{(1+|\alpha\ h_w|^{\eta})^{m+1}} \tag{4}$$

$$K_w=K_{ws}S_e^{0.5}[1-(1-S_e^{1/m})^m]^2 \tag{5}$$

where S_e is the effective saturation; α and η are empirical parameters; θ_s and θ_r are saturated and residual moisture content, respectively; n is the porosity of soil; K_{ws} is the saturated hydraulic conductivity; and $m = 1 - 1/\eta$.

To analyze 3D water-air two-phase seepage-flow, the following equations were derived for the simultaneous flow of water and air based on one-dimensional (1D) flow equations (Touma and Vauclin, 1986).

Water-phase Eq. (6):

$$C_c\left(\frac{\partial h_a}{\partial t}-\frac{\partial h_w}{\partial t}\right)=\frac{\partial}{\partial x}\left(K_{wx}\frac{\partial h_w}{\partial x}\right)+\frac{\partial}{\partial y}\left(K_{wy}\frac{\partial h_w}{\partial y}\right)+\frac{\partial}{\partial z}\left(K_{wz}\left(\frac{\partial h_w}{\partial z}+1\right)\right) \tag{6}$$

Air-phase Eq. (7):

$$\left((n-\theta_w)\frac{\rho_{oa}}{h_o}-\rho_aC_c\right)\frac{\partial h_a}{\partial t}+\rho_aC_c\frac{\partial h_w}{\partial t}=\frac{\partial}{\partial x}\left(\rho_aK_{ax}\frac{\partial h_a}{\partial x}\right)+\frac{\partial}{\partial y}\left(\rho_aK_{ay}\frac{\partial h_a}{\partial y}\right)+\frac{\partial}{\partial z}\left(\rho_aK_{az}\left(\frac{\partial h_a}{\partial z}+\frac{\rho_a}{\rho_{ow}}\right)\right) \tag{7}$$

where h_a is the air pressure head; h_o is the atmospheric pressure expressed in terms of water column height; $C_c=\partial\theta_w/\partial h_c$ is the capillary capacity; $h_c = h_a - h_w$ is the capillary head; n is the porosity of the soil; ρ_a is the density of the air; ρ_{oa} is the density of the air at atmospheric pressure; ρ_{ow} is the density of the water at atmospheric pressure; and K_{ax}, K_{ay}, and K_{az} are the air conductivity in the x, y, and z directions, respectively.

In order to solve Eqs. (6) and (7), the following constitutive relationships were used.

van Genuchten (1980) proposes the following relationships:

$$S_e=[1+(\alpha h_c)^{\eta}]^{-m} \tag{8}$$

$$C_c=\frac{(n-\theta_r)\ \eta\ m\ \alpha\ (\alpha\ h_c)^{\eta-1}}{(1+(\alpha\ h_c)^{\eta})^{m+1}} \tag{9}$$

Chen *et al.* (1999) used the following relationship as the Van Genuchten and Mualem (VGM) model:

$$K_a=K_{as}S_e^{0.5}(1-S_e)^{0.5}[(1-S_e^{1/m})]^{2m} \tag{10}$$

where $K_{as} = K_{ws} \times (\mu_w/\mu_a)$ is the saturated air conductivity; and

μ_w and μ_a are the dynamic viscosity of water and air, respectively. $\mu_w = 1.002 \times 10^{-2} NS/m$ and $\mu_a = 1.83 \times 10^{-5} NS/m^2$ at 20°C.

Eqs. (1), (6), and (7) were solved by a line-successive over-relaxation (LSOR) scheme with an implicit iterative finite difference scheme as used by Freeze (1978).

2.2 Surface Flow and Erosion/deposition Model

The mathematical model developed by Takahashi and Nakagawa (1994) was used to investigate the surface flow and erosion/deposition on the surface of the model slope. The depth-wise averaged 2D momentum equations for the x-wise (down valley) and y-wise (lateral) directions are:

$$\frac{\partial M}{\partial t} + \beta\frac{(\partial uM)}{\partial x} + \beta\frac{(\partial vM)}{\partial y} = gh\sin\theta_{bxo} - gh\cos\theta_{bxo}\frac{\partial(h+zb)}{\partial x} - \frac{\tau_{bx}}{\rho_T} \tag{11}$$

and

$$\frac{\partial N}{\partial t} + \beta\frac{\partial(uN)}{\partial x} + \beta\frac{\partial(vN)}{\partial y} = gh\sin\theta_{byo} - gh\cos\theta_{byo}\frac{\partial(h+z_b)}{\partial y} - \frac{\tau_{by}}{\rho_T} \tag{12}$$

The continuity equation of the total volume is:

$$\frac{\partial h}{\partial t} + \frac{\partial M}{\partial x} + \frac{\partial N}{\partial y} = i_b\{c_* + (1-c_*)s_b\} + R - I \tag{13}$$

The continuity equation of the particle fraction is:

$$\frac{\partial(ch)}{\partial t} + \frac{\partial(cM)}{\partial M} + \frac{\partial(cN)}{\partial y} = i_b c_* \tag{14}$$

The equation for the change of bed surface elevation is:

$$\frac{\partial z_b}{\partial t} = -i_b \tag{15}$$

where M (=uh) and N (=vh) are the flow discharge per unit width in the x and y directions; u and v are depth-averaged velocities in the x and y directions, respectively; h is the water depth; g is the gravitational acceleration; β is the momentum correction factor; θ_{bxo} and θ_{byo} are the x and y components of the slope of the original bed surface; ρ_T is the mixture density; τ_{bx} and τ_{by} are the bottom shear stresses in the x and y directions, respectively; R is the rainfall intensity; I is the infiltration rate; s_b is the degree of saturation in the bed; i_b is the rate of hydraulic erosion or deposition from the flowing water (rate of splash erosion was not considered); c is the sediment concentration in the flow; c_* is the maximum sediment concentration in the bed; and z_b is the erosion or deposition thickness measured from the original bed elevation. Using the following relationships, s_b and I were obtained through seepage analysis: $s_b = \theta_w/\theta_s$ for top cell. If $h > 0$, then $I = K_{ws}(\partial h_w/\partial z + I)$ of the top cell; otherwise, $I = R$.

The erosion and deposition rate given by Takahashi (1991) are expressed in Eqs. (16) and (17), respectively.

$$\frac{i_b}{\sqrt{gh}} = K_e\sin^{3/2}\theta_b\left\{1 - \frac{\sigma-\rho_T}{\rho_T}c\left(\frac{\tan\phi}{\tan\theta} - 1\right)\right\}^{1/2} \cdot \left(\frac{\tan\phi}{\tan\theta} - 1\right)(c_\infty - c)\frac{h}{d_m} \tag{16}$$

$$i_b = \delta_d\frac{c_\infty - c}{c_*}\sqrt{u^2 + v^2} \tag{17}$$

where ϕ is the internal friction angle of the bed; K_e is the parameter of erosion velocity; θ_b is the bed slope; σ is the density of the sediment particles; $\tan\theta$ is the gradient of the energy slope; d_m is the mean particle size; δ_d is a constant; and c is the equilibrium solids concentration described as follows (Nakagawa *et al*., 2003).

If $\tan\theta > 0.138$,

$$c_\infty = \frac{\rho\tan\theta}{(\sigma-\rho)(\tan\phi - \tan\theta)} \tag{18}$$

If $0.03 < \tan\theta \le 0.138$,

$$c_\infty = 6.7\left\{\frac{\rho\tan\theta}{(\sigma-\rho)(\tan\phi - \tan\theta)}\right\}^2 \tag{19}$$

If $\tan\theta \le 0.03$,

$$c_\infty = \frac{(1+5\tan\theta)\tan\theta}{\sigma/\rho - 1}\left(1 - \alpha_0^2\frac{\tau_{*c}}{\tau_*}\right)\left(1 - \alpha_0\sqrt{\frac{\tau_{*c}}{\tau_*}}\right) \tag{20}$$

where τ_* is the non-dimensional shear stress; τ_{*_c} is the non-dimensional critical shear stress; and

$$\alpha_0^2 = \frac{2\{0.425 - (\sigma/\rho)\tan\theta/(\sigma/\rho - 1)\}}{1 - (\sigma/\rho)\tan\theta/(\sigma/\rho - 1)} \tag{21}$$

$$\tau_* = \frac{h\tan\theta}{(\sigma/\rho - 1)d_m} \tag{22}$$

$$\tau_{*_c} = 0.04 \times 10^{1.72\tan\theta} \tag{23}$$

If $\tan\phi \le \tan\theta$ in Eq. (18), $c_\infty = c = 0.9 \times c_*$ in Eq. (16) and consequently $i_b = 0$. If $c = c_\infty$ in Eq. (16), $i_b = 0$ and no erosion takes place. If $c > c_\infty$, deposition takes place, and Eq. (17) gives the deposition rate.

The finite difference form of Eqs. (11) to (14) were obtained by the solution methods developed by Nakagawa (1989) using the Leap-Frog scheme.

2.3 Slope Stability Model

The limit equilibrium method of slices was used for slope stability analysis. Janbu's simplified method and the extended Spencer method have been incorporated into an effective minimization procedure based on dynamic programming by which the minimal factor of safety and the corresponding critical non-circular slip surface are determined simultaneously.

Awal *et al.* (2009) used the following expression of Janbu's simplified method to determine the factor of safety F_s.

$$F_s = \frac{\sum[(c_e - u_p\tan\phi)\Delta x\Delta y + (W+P)\tan\phi]/[(1/J + \sin\alpha_{xZ}\tan\phi/F_S)\cos\alpha_{xz}]}{\sum(W+P)\tan\alpha_{xz}} \tag{24}$$

where, $J = (1 + \tan^2\alpha xz + \tan^2\alpha yz)^{1/2}$; W is the weight of a column; P is the vertical external force acting on the top of the column; u_p

is the pore water pressure at the base of the column; x and y are discretized widths of the columns in the x and y directions, respectively; Δ_{xz} and Δ_{yz} are the inclination angles of the column base to the horizontal direction in the xz and yz planes, respectively; and c_e is the effective cohesion.

The following equations for the factors of safety for the extended Spencer method were used (Jiang and Yamagami, 2004).

$$F_f = \frac{\sum\left[\begin{array}{c}(c_e - u_p\tan\phi)\sec\alpha_{xz}\Delta x\Delta y + (W+P)\\ (\sec\alpha_{xz} - \tan\delta\sin\alpha_{xz})\tan\phi + F_f\tan\delta\tan^2\alpha_{xz}/J\end{array}\right]/m_\alpha}{\sum(W+P)\tan\alpha_{xa}} \quad (25)$$

$$F_m = \frac{\Sigma D\left[\begin{array}{c}(c_e - u_p\tan\phi)\sec\alpha_{xz}\Delta x\Delta y\sin(\theta_d+\delta)/\cos\theta\\ +(W+P)\cos(\theta_d+\alpha_{xz})\\ \{\tan\phi\tan(\theta_d+\alpha_{xz})F_m\sec\alpha_{xz}/J\}\end{array}\right]/m_\alpha}{\sum(W+P)D\cos\theta_d} \quad (26)$$

where F_f and F_m are the factors of safety with respect to force equilibrium and moment equilibrium, respectively; $m_\alpha = (1+\tan\alpha\tan\delta_{xz})/J + (\sin\alpha_{xz} - \tan\theta\cos\alpha_{xz})\tan\phi/F$, with $F = F_f$ for Eq. (25) and F_m for Eq. (26); δ is the inclination of interslice forces to the horizontal; D is the distance from the axis of rotation to the base center of a column in the xz plane; and δ_d is the angle between the horizontal direction and the D direction in the xz plane.

F_f and F_m can separately be computed from Eqs. (25) and (26) for several appropriately given values of δ. Then, two curves showing the relationships of F_f - δ and F_m - δ can be plotted so that the intersection of these two curves leads to a required δ_o value and corresponding factor of safety F_s, satisfying both force and moment equilibria.

3. Experimental Study

3.1 Rainfall-induced Slope Failure

A 3 m long, 80 cm wide and 70 cm deep rectangular flume with an adjustable longitudinal slope was used for the experiment. The flume sidewalls were made of aquarium glass. To capture the initiation of the slope failure process and movement of the failure mass, three digital Video Cameras (VCs) were used. Two cameras were placed in the sides and one was placed in the front of the flume. The experiments were carried out on 23° and 28° flume slopes.

It is difficult to observe the 3D view of the failure surface in the rectangular flume shape. So, the rectangular shape of the flume was modified using 292.5 cm long and 3cm thick wooden plates to make a V-shape valley cross section having a cross slope of 20°. Slope failures can be rapid and devastating on steep slopes and can be imperceptibly slow in the gentle slope. Therefore, a comparatively steeper slope was provided in the sloping face of the model slope. Hence, in the down slope direction its thickness is of tapered shape. The model slope was prepared on the rigid bed of the flume by placing medium-grained silica sand S6.

A small space was allowed in the upstream for providing runoff input so as to develop a water table in the bottom layer of the model slope, which is essential for understanding the slope failure phenomenon. The downstream end of the flume was closed with a filter mat supported by a wooden plate to retain the soil and provide downstream free flow conditions. The downstream seepage outflow was collected in a measuring cylinder through a metal container. Profile Probes (PRs) consisting of four sensors (SRs) were used to measure the temporal variation of moisture content, and Pressure Transducers (PTs) were used to measure the temporal variation of air pressure at different locations inside the body of the model slope. Red-colored sediment strips and red-colored cotton threads were placed respectively at the side wall faces and inside the body, normal to the flume bed, so as to measure the failure surface after sliding. Measuring scales were placed in vertical position on the top surface of the model slope in its central longitudinal section to measure the forefront of the propagated surface water flow. The schematic diagram of the flume including instrumentation and data acquisition system is shown in Fig. 1. The shape and size of the model slope with the arrangement of SRs, PTs, and surface water forefront measurement scales are shown in Figs. 2 and 3. Some parameter values of the

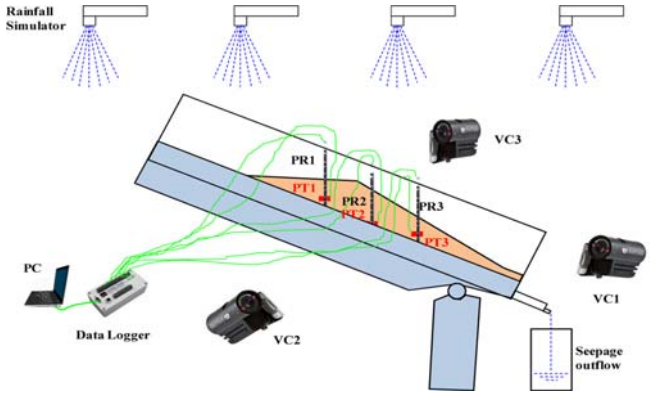

Fig. 1. The Schematic Diagram of the Flume Including Instrumentation and Data Acquisition System

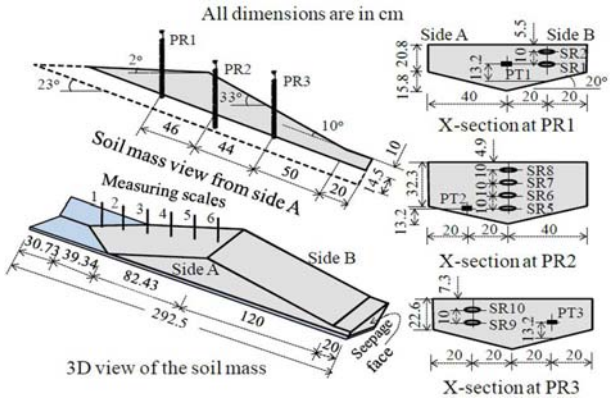

Fig. 2. Model Slope with the Arrangement of SRs, PTs, and Surface Water Forefront Measurement Scales (Flume Slope 23°)

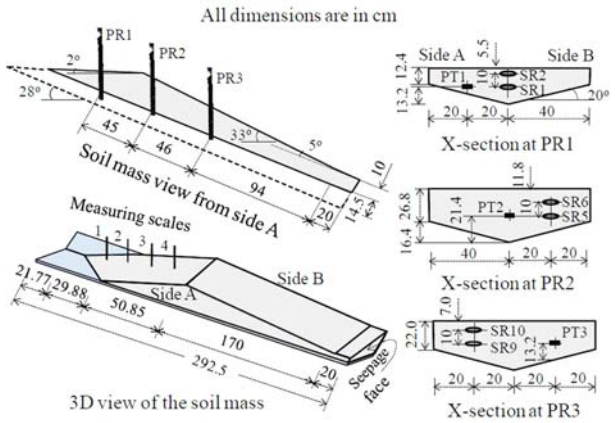

Fig. 3. Model Slope with the Arrangement of SRs, PTs, and Surface Water Forefront Measurement Scales (Flume Slope 28°)

Table 1. Some Parameter Values of the Sediments Considered

Sediment type	S6	Smix
Saturated moisture content, θ_s	0.42	0.287
Residual moisture content, θ_r	0.004	0.045
van Genuchten parameter, α	3.227	5.50
van Genuchten parameter, η	2.7	3.20
Specific gravity, G_s	2.63	2.65
Mean grain size, D50 (mm)	0.24	1.0
Angle of repose, ϕ	34^0	34^0
Porosity, n	0.42	0.345
Compression index, CI	1.08	1.11

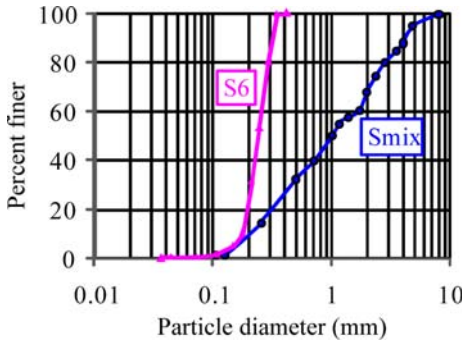

Fig. 4. Grain Size Distribution of the Sediment

sediment used in the experiments are listed in Table 1. The grain size distributions of the sediment are shown in Fig. 4.

In the experiment, the artificial rainfall over the flume, provided by the simulators, was not uniform. Also the measured rainfall values at the same location were different in different measurements. This unreliability in rainfall intensity was due to power fluctuation in the water pump, losses in water supply pipes, temperature variations, etc. Unreliability of rainfall leads to weaken the experimental results. To measure rainfall intensity, five experiments were conducted with the same supply condition of the water pump, 98 liters per minute, in different seasons throughout a year. In each rainfall measurement experiment, 24 buckets having opening diameter 207.5 mm were placed inside the flume, to collect rainfall water. The buckets were arranged in three rows (8 buckets in each row) with equal spacing, and their

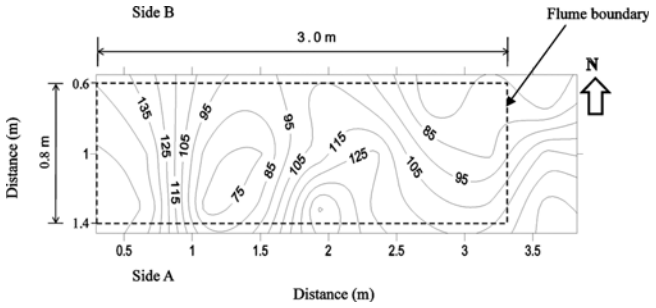

Fig. 5. Distribution of Rainfall Intensity (mm/hr) Over the Flume

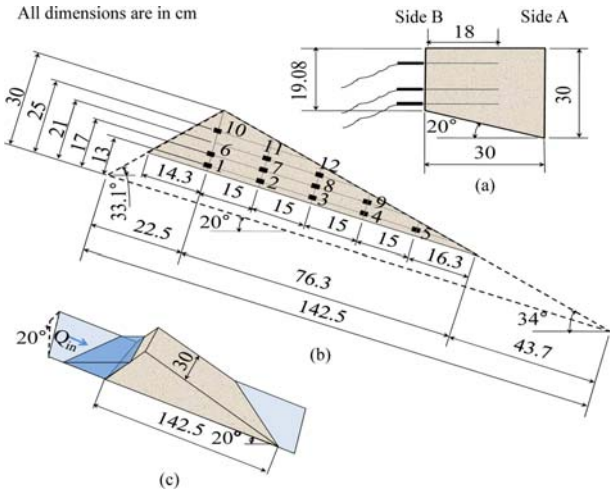

Fig. 6. Landslide Dam Body Shape and Size with the Arrangements of WCRs (1-12): (a) X-section at Crest, (b) WCRs arrangement, View from Side B, (c) 3D View of the Dam Body

position was always same for each rainfall measurement experiment. The duration of the rainfall measurement was 15 to 20 minutes. The average value of these measurements was 105.03 mm/hr, which was assumed as the supply rainfall value in experiments and simulations. Fig. 5 presents a contour map showing rainfall distribution over the flume.

3.2 Landslide Dam Failure

Experimental results obtained by Awal *et al.* (2009) were compared with the simulation results. They used a rectangular flume of length 500 cm, width 30 cm and depth 50 cm set at 20° longitudinal slope in their landslide dam experiment. It is difficult to observe the 3D view of the failure surface in a rectangular flume shape. So, the rectangular shape of the flume was modified to make a cross slope of 20°. A triangular dam was prepared on the rigid bed of the flume by placing mixed sediment Smix (silica sand Mix 1-7) on the flume. Water Content Reflectometers (WCRs) were used to measure the temporal variation of the moisture content during the seepage process. The shape and size of the landslide dam with the arrangement of WCRs are schematically shown in Fig. 6. During the experiment, 29.8 cm^3/sec steady discharge was supplied from

upstream of the flume. Some parameter values of the sediment used in the experiment are listed in Table 1. The grain size distribution of the sediment is shown in Fig. 4.

4. Results and Discussions

4.1 Rainfall-induced Slope Failure

In the seepage-flow model, the numerical simulation was conducted at 0.01-sec time steps and 2.5-cm space steps in the x (longitudinal), y (lateral), and z (vertical) directions. The x and y directions were assumed to be horizontal. In the surface-water flow and erosion/deposition models, 0.005-sec time steps and 2.5-cm space steps in the x (parallel to longitudinal axis of flume) and y (horizontal) directions were used. Time steps of 10 sec and space steps of 10 cm in the horizontal x and y directions were used in the slope-stability model. The parameters of the numerical simulation were: $K_{wx} = K_{wy} = K_{wz} = K_w$, $K_{ax} = K_{ay} = K_{az} = K_a$, $K_{ws} = 0.0002153$ m/sec; $h_o = 10.336$ m; $g = 9.81$ m/sec^2; $\rho_T = \rho_{ow} = 1000.0$ kg/m^3; $\rho_{oa} = 1.275$ kg/m^3; $\beta = 1.25$; $c_* = 0.5779$; $K_e = 0.06$; $\sigma = 2630$ kg/m^3; $\delta_d = 0.03$; and $S_s = 1 \times 10^{-7}$ m^{-1} (for the saturated condition of the sediment).

The electromagnetic field of the profile probe sensors extended up to 60 mm into the soil. The influence of SR8 and SR10 (23° flume slope case) and the influence of SR6 and SR10 (28° flume slope case) reached up to the soil surface in the sloping face of the model slope (Figs. 2 and 3). The moisture profiles in experiments and simulations did not matching well for these sensors (Figs. 7 and 8). However, the profiles of the other sensors were comparable.

Air became trapped in the voids by the water infiltrating from the surface, initially compressing the air phase and reducing the rate of water infiltration. The air pressure increased until it was sufficient for the air to escape via bubbling. The moisture profiles obtained from the two-phase flow were delayed slightly compared with those for the one-phase flow (Figs. 7 and 8). Fig. 9 compares the experimental and simulated air-pressure-head profiles at different PTs. The experimental and simulated seepage outflows from the downstream seepage face are shown in Fig. 10. Table 2 compares the experimental and simulated surface-water forefront propagation time at different measurement scales.

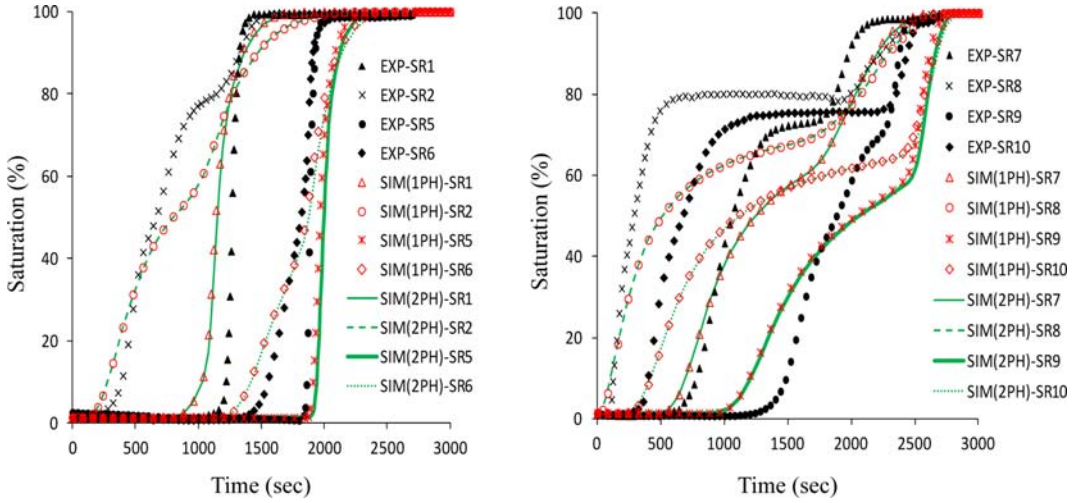

Fig. 7. Simulated and Experimental Moisture Content Profiles (23° Flume Slope)

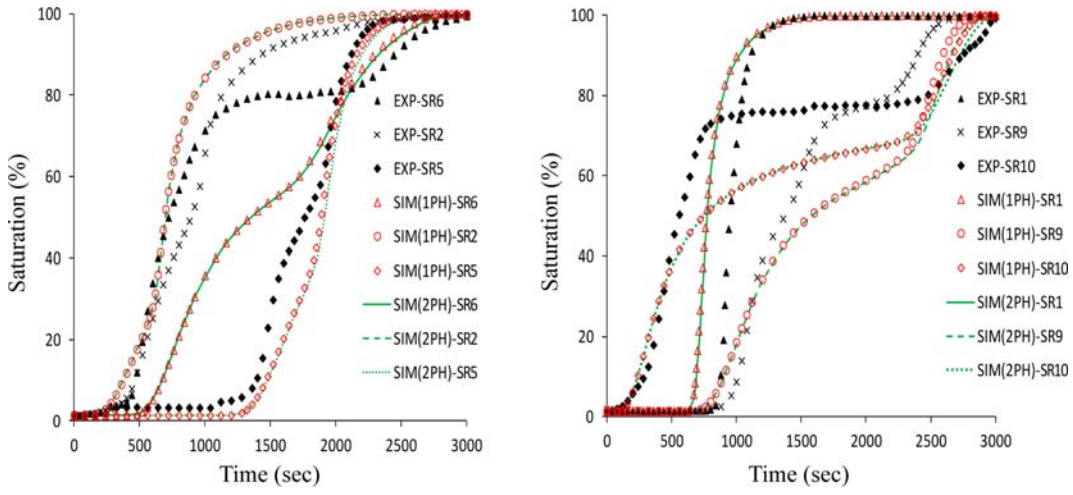

Fig. 8. Simulated and Experimental Moisture Content Profiles (28° Flume Slope)

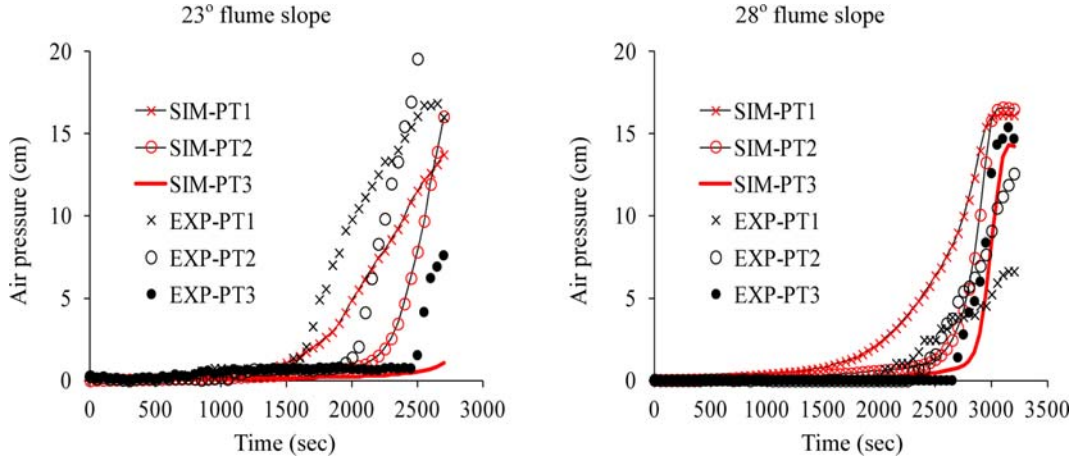

Fig. 9. Simulated and Experimental Air Pressure Head Profiles

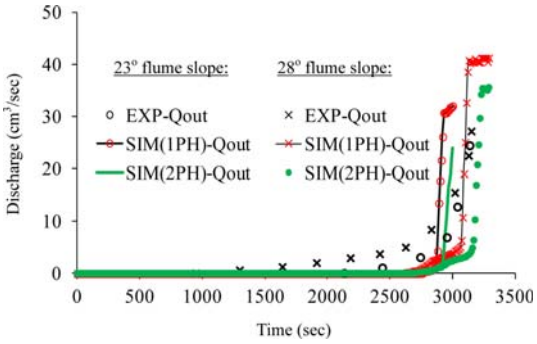

Fig. 10. Seepage Outflow

Table 2 Surface Water Forefront Propagated Time to Measuring Scales

Scale	Distance Parallel to flume slope (m)	Water forefront reached time (sec) EXP	Water forefront reached time (sec) SIM-1PH	Water forefront reached time (sec) SIM-2PH
23° flume slope				
1	2.5	35	28	28
2	2.3	77	111	113
3	2.1	276	374	359
4	1.9	761	975	951
5	1.7	1369	1587	1527
6	1.5	1983	2192	2138
28° flume slope				
1	2.6	102	94	92
2	2.45	497	436	422
3	2.3	2153	1832	1646
4	2.15	3184	2788	2788

Table 3. Summary of the Slope Stability Analysis

Seepage Analysis	Simulation				Experiment
	Slope stability analysis method				
	Janbu's simplified		Extended Spencer		
	Failure time (sec)	Fs	Failure time (sec)	Fs	Failure time (sec)
23° flume slope					
1PH	2780	0.996	2820	0.984	2779 (EXP-D) 2830 (EXP-E)
2PH	2830	0.992	2850	1.000	
28° flume slope					
1PH	3020	0.994	3060	0.948	3286
2PH	3100	0.979	3140	0.964	

In most of the cases these simulation results were comparable with the experimental data.

The effect of unreliable rainfall supply is evident in the comparison of the experimental and simulation results. For the 23° flume slope, full saturation of the moisture profiles was delayed in the simulations compared with the experiments for almost all of the sensors (Fig. 7). Additionally, the air-pressure-head profiles (Fig. 9) and surface-water forefront propagation (Table 2) were delayed in the simulations. For the 28° flume slope, most of the sensors indicated that full saturation of the moisture profiles occurred earlier in the simulations than the experiments showed (Fig. 8). The air-pressure-head profiles, except PT3 (Fig. 9), and surface-water forefront propagation (Table 2) were faster in the simulations. Because PT3 was located near the downstream end of the model slope and surface water did not propagate into this reach, the simulation air-pressure-head profile in this position was influenced only by the localized rainfall intensity above it. This localized rainfall intensity in the simulations might have been less than the actual value.

For the 23° flume-slope experiments were conducted in winter, whereas the 28° flume-slope experiments were conducted in summer. Furthermore, the failure times of the model slopes were, on average, delayed in simulations compared with the experiments for the 23° flume slope and accelerated in the simulations compared with the experiments for the 28° flume slope (Table 3). Due to the reduction in the water-infiltration rate caused by the air phase, the surface-water forefront propagation in a two-phase simulation should be faster than that in a one-phase simulation. However, in some stages of the surface-water forefront, the degree of soil saturation just below the forefront is

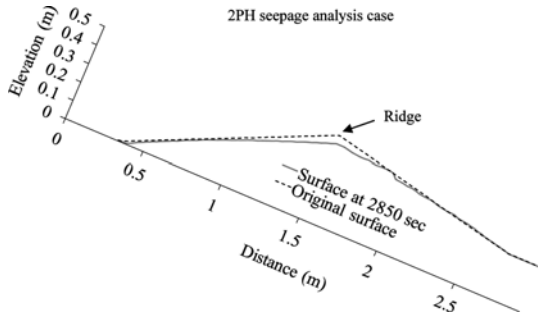

Fig. 11. Original and Simulated Soil Surface at Longitudinal Section through Center Line (23° Flume Slope)

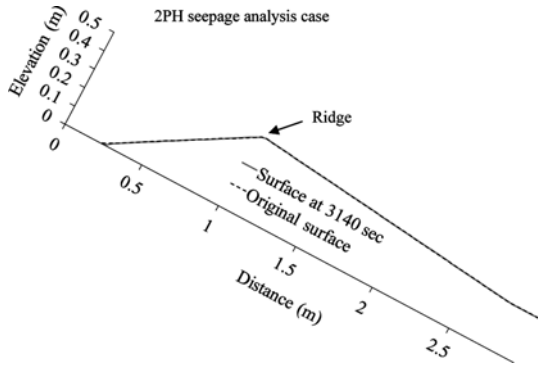

Fig. 12. Original and Simulated Soil Surface at Longitudinal Section through Center Line (28° Flume Slope)

reduced due to a delay in the lateral movement of seepage water from upstream. In such stages, the infiltration rate from the surface is higher, so the propagation rate can be delayed substantially. At measuring scale 2 for the 23° flume slope (Table 2), the surface-water propagation time was delayed somewhat in the two-phase flow compared with the one-phase flow. At measuring scale 4 for the 28° flume slope (Table 2), the surface-water propagation time was the same in the two-phase and one-phase simulations. At the other scale positions, the surface-water propagation time was faster in the two-phase flow than in the one-phase flow.

Figures 11 and 12 compare the soil-surface profiles obtained from the simulations at the time of failure in the model slopes, considering the two-phase seepage-flow analysis, with the original soil surface at the longitudinal section through the center line. In the 23° flume slope, the area upstream from the model slope was comparatively larger than that for the 28° flume slope (Figs. 2 and 3). The runoff input of the model slope for the former was greater than that for the latter. Due to the smaller flume slope, the vertical distance traveled by the infiltrating

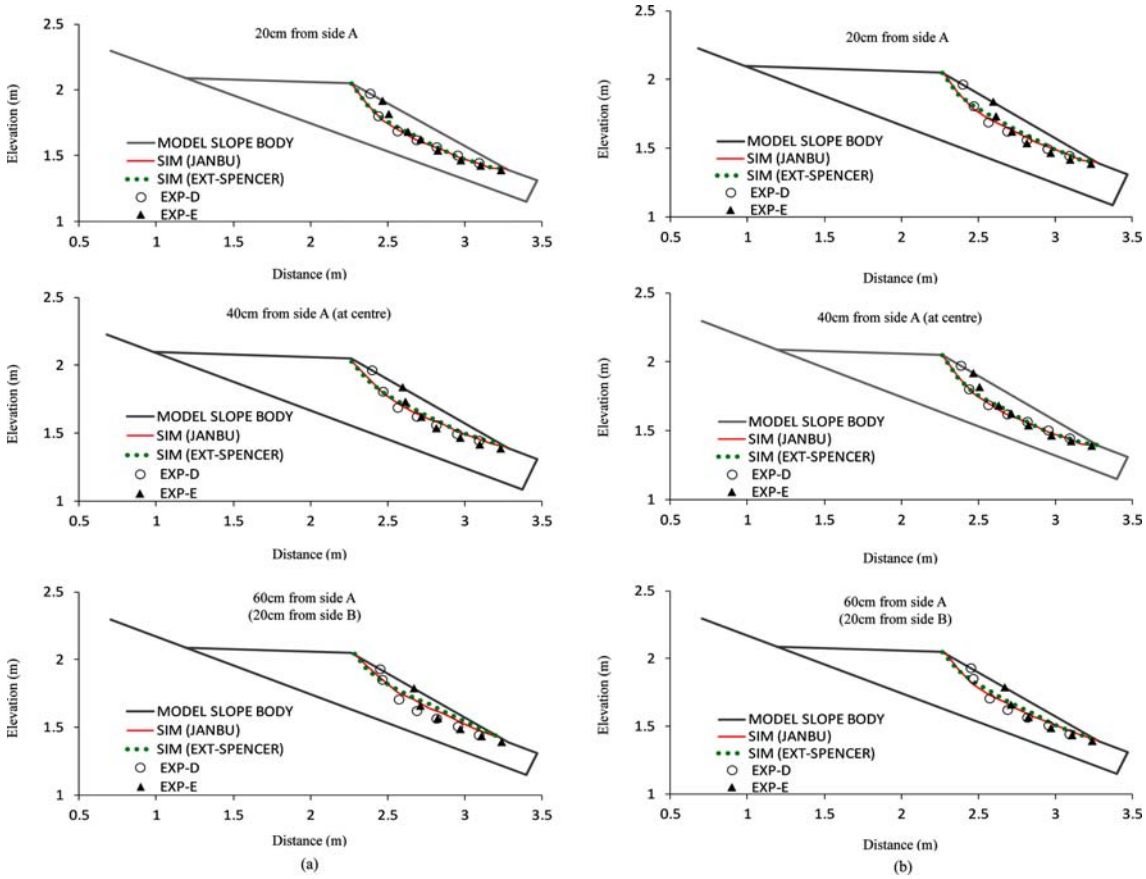

Fig. 13. Comparison of Longitudinal Profiles of Experimental and Simulated Failure Surfaces for: (a) 1PH Seepage Analysis Case (23° Flume Slope), (b) 2PH Seepage Analysis Case (23° Flume Slope)

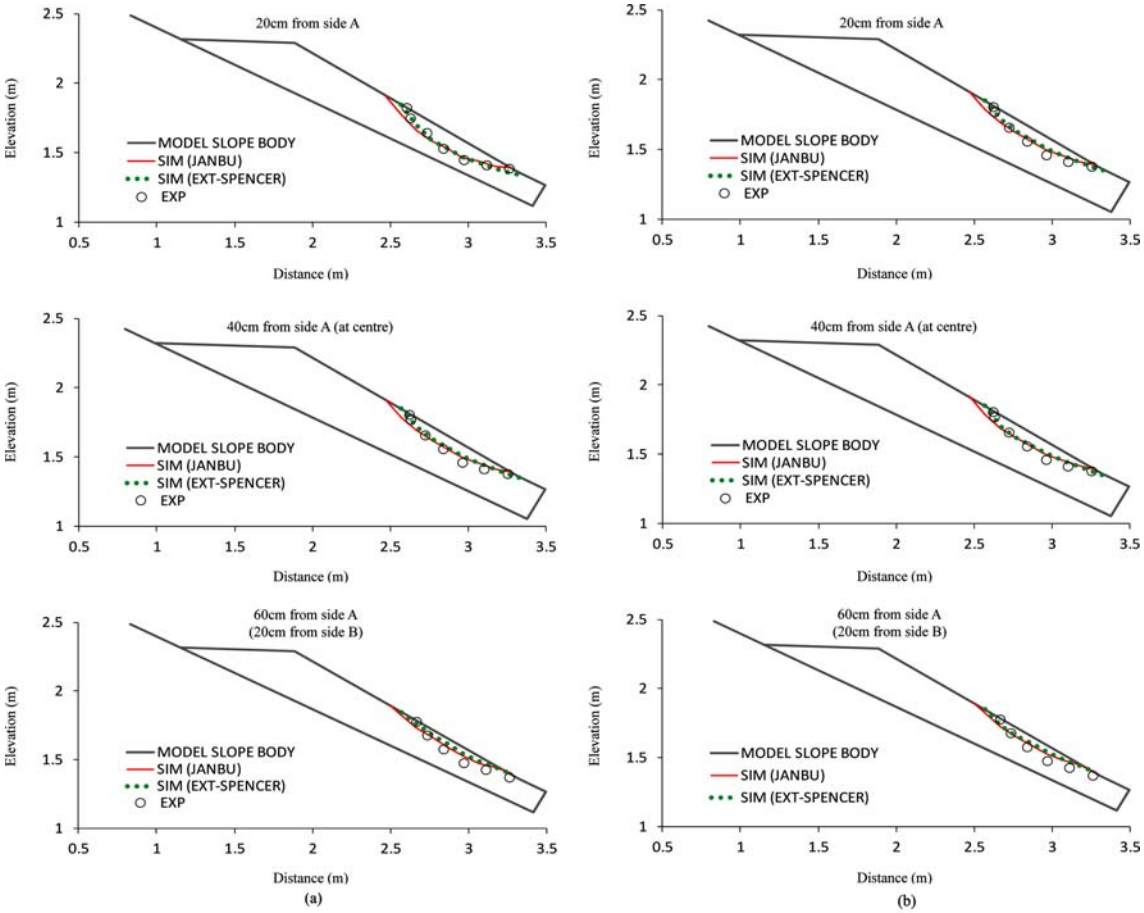

Fig. 14. Comparison of Longitudinal Profiles of Experimental and Simulated Failure Surfaces for: (a) 1PH Seepage Analysis Case (28° Flume Slope), (b) 2PH Seepage Analysis Case (28° Flume Slope)

less in the former than the latter, so the particular depth was saturated earlier in the former. Therefore, the surface-water flow was faster in the 23° flume slope than in the 28° flume slope; it crossed the ridgeline before the failure of the model slope, and significant erosion occurred in the simulations (Fig. 11). By contrast, in the 28° flume slope, the surface water flow did not cross the ridgeline before the failure, and no erosion was observed in the simulations (Fig. 12).

The time of failure of the model slope and the corresponding safety factor calculated by different methods in different cases are summarized in Table 3. Fig. 13(a), Fig. 13(b), Fig. 14(a), and Fig. 14(b) show the failure surfaces obtained from the simulations and experiments in longitudinal profile. Fig. 15 presents a 3D view of the failure surface observed in experiment D and computed using the extended Spencer method considering two-phase flow for the 23° flume slope. Similarly, Fig. 16 presents a 3D view of the failure surface observed in an experiment and computed with the extended Spencer method considering two-phase flow for the 28° flume slope. The comparison indicated that the simulated and experimental failure surfaces, as well as the corresponding times of failure, matched well. The failure time of the numerical analysis corresponded to

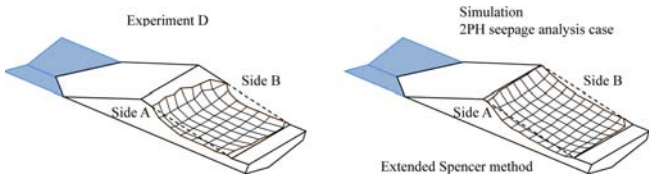

Fig. 15. 3D View of Failure Surface (23° Flume Slope)

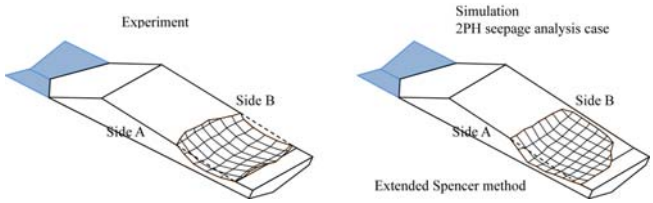

Fig. 16. 3D View of Failure Surface (28° Flume Slope)

the time at which the computed $F_s \leq 1.0$. Although a slope-stability simulation is possible for each time step of the seepage analysis, 10-sec time steps were used to reduce the simulation duration. Therefore, the F_s values in the different simulations were not the same. In the experiment, the moment of failure of the model slope was judged from the recorded video clips.

Because the overall rainfall intensity was more intense on side A than on side B (Fig. 5), the observed sliding slope with a deeper failure surface was concentrated on side A in the experiments as well as the simulations. Nearer side B, the failure surface predicted by the simulation was shallower than that observed experimentally in both cases. However, the failure plane in the simulation was not observed at side B in the 28° flume slope (Fig. 16). These phenomena are explained by the unreliable rainfall supply, mentioned above. There must be some deposition in the toe of the model slope after failure. However, to predict the deposition, a model must be developed to determine the distance moved by the failure mass and its shape and size after movement. Therefore, Figs. 15 and 16 present only the failure surface in the original shape of the model slope.

Worldwide, slopes exist in residual soil deposits. These soils are often unsaturated, and the conventional approach that assumes only water-phase flow in seepage analysis is inadequate. To improve seepage analyses, a water-air two-phase flow model has been used to consider the air movement phenomenon inside the body of the model slope. The simulated moisture profiles from the water-air two-phase seepage-flow models occurred slightly after those of the conventional seepage-flow models (Figs. 7 and 8). Ultimately, the failure time of the slope body was delayed using Janbu's simplified method and the extended Spencer method (Table 3). However, only for the 28° flume slope, the failure times from the two-phase flow model were closer to the values observed experimentally compared with those from the one-phase flow model. To improve this modeling approach, additional experimental verifications in different soils and field applications are necessary.

Janbu's simplified method satisfies only the force equilibrium for the entire sliding mass and assumes that the resultant interslice forces are horizontal, whereas the extended Spencer method satisfies both the force and moment equilibria and assumes that the resultant interslice forces are at an angle to the horizontal. Due to the vertical component of inclined interslice forces, the calculated mobilized shear stress using the extended Spencer method is less than that of Janbu's simplified method at a given moisture content. Therefore, the safety factor calculated using Janbu's simplified method was less than that from the extended Spencer method, resulting in a delayed failure time for the body of the model slope compared with Janbu's simplified method.

4.2 Landslide Dam Failure

In the seepage flow model, numerical simulation was carried out with time steps of 0.01 second and space steps of 1.0 cm in x (longitudinal), y (lateral), and z (vertical) directions. Time steps of 1.0 second and space steps of 5 cm in x (longitudinal) and 3 cm in y (lateral) directions were used in the slope stability model. Both x and y directions were assumed to be horizontal.

Figure 17 shows the comparison of experimental and simulated moisture profiles at WCRs 2, 4, and 8 which are in good agreement with attainment of full saturation that is found to be earlier in all WCRs in simulated results rather than

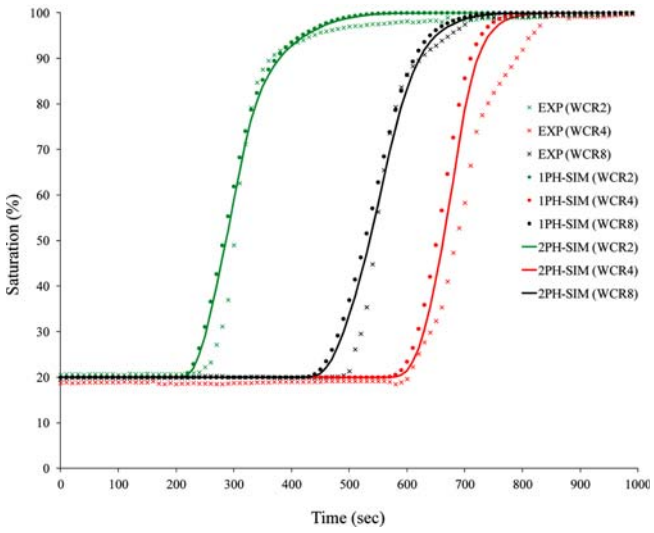

Fig. 17. Experimental and Simulated Moisture Profiles

experimental. Table 4 presents the summary of the slope stability analysis. Figs. 18(a) and 18(b) show the comparison of experimental and simulated critical slip surfaces. In side A of the dam body, the computed slip surface is very close to the experimentally observed slip surface, whereas in side B the computed slip surface is shallower than that of the experimentally observed surface.

The positions of WCRs 2, 4, and 8 are closer to the head reach than the tail reach of the dam body. Earlier saturation of these WCRs in simulations (Fig. 17) indicates that the head reach of the dam body saturated faster and the tail reach saturated more slowly in simulations than in experiments, in a given upstream discharge condition. This means that the simulated upstream reservoir level rising rate was faster than the experimental rate. Since the dam body mass in the head reach is dominant for the slope failure, numerically obtained slope failure will be earlier and shallower than experimentally obtained data due to such phenomenon. However, in the present study, the numerically obtained failure surface is shallower only in side B. The friction on the side wall of the flume was ignored in the computation. Since the dam body contact area to the flume side wall is greater in side A than side B, the effect of friction in computation will be more significant in side A than that of side B, resulting in the deeper slip surface computed in side A as closer to the experimental one. Fig. 19 presents a 3D view of the failure surface computed by the extended Spencer method considering two-phase flow.

The water level rising rate upstream of the dam body depends on the rate of moisture movement inside the dam. The saturated hydraulic conductivity K_s and the van Genuchten parameters (α and η), which depend on the sand mix and its compaction, are the key parameters for guiding moisture movement and consequently failure time of the dam. It is difficult to ensure uniformity of sand mix and its compaction while determining these parameters and formation of the experimental dam body. It is necessary to record

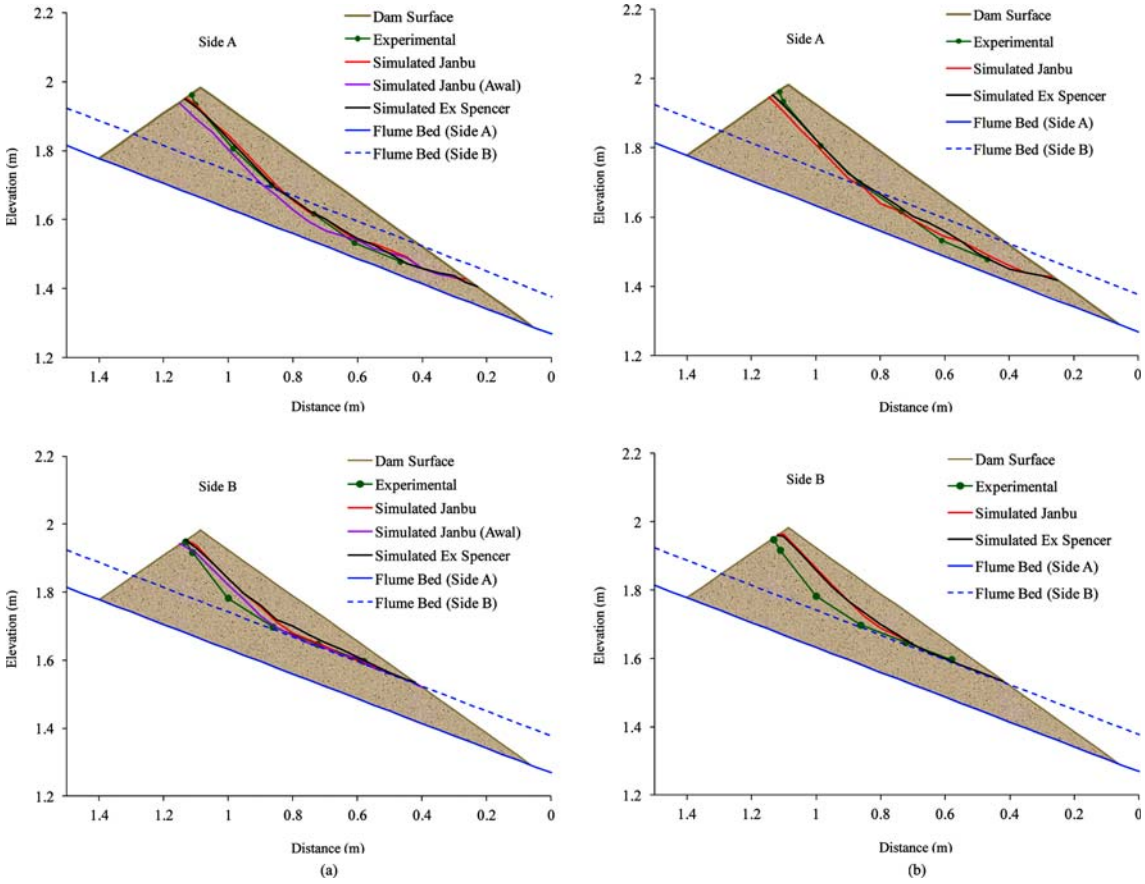

Fig.18. Experimental and Simulated Critical Slip Surfaces for: (a) 1PH Seepage Analysis Case, (b) 2PH Seepage Analysis Case

Table 4. Summary of the Slope Stability Analysis

Seepage Analysis	Simulation				Experiment
	Slope stability analysis method				
	Janbu's simplified		Extended Spencer		
	Failure time (sec)	F_s	Failure time (sec)	F_s	Failure time (sec)
1PH	768	0.999	793	0.999	930
2PH	777	0.998	802	0.997	
1PH (Awal *et al.*, 2009)	770	0.991	-	-	

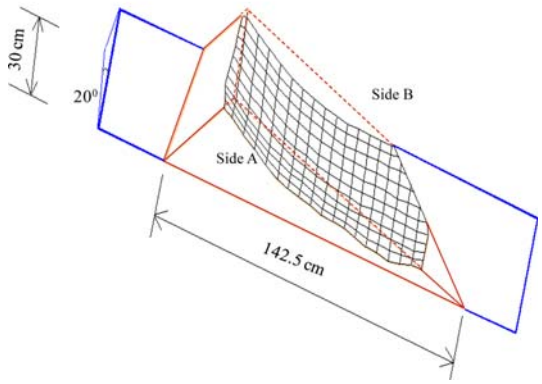

Fig. 19. 3D View of Failure Surface, Computed by Extended Spencer Method (2PH Seepage Consideration)

the temporal variation of the upstream reservoir level during experiments so that the value of these parameters can be optimized to get a more accurate simulated reservoir level that may lead to simulated moisture movement, dam body failure time, and shape of the failure surface that are quite close to the experimental ones.

Since the water-air two-phase flow model was used to consider the air movement phenomenon inside the dam during the seepage process, as in the case of rainfall-induced slope failure, simulated moisture profiles obtained by the water-air two-phase seepage flow model were slightly delayed compared to those obtained using the conventional seepage flow model (Fig. 17). Ultimately, failure time of the dam body was also found to be delayed when using Janbu's simplified method as well as the extended Spencer method (Table 4). As in the case of rainfall-induced slope failure, the factor of safety calculated by Janbu's simplified method is less than that of the extended Spencer method, resulting in a failure time of the landslide dam delayed in the extended Spencer method than Janbu's simplified method.

Considering two-phase flow seepage analysis simulations were also carried out to analyze the sensitivity of dam body stability to the K_s value parameter, the K_s value was varied by

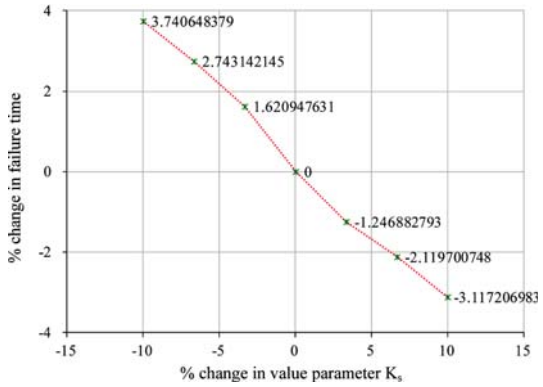

Fig. 20. Sensitivity of Dam Stability to Variation on K_s (2PH Seepage Consideration)

±10%, so that its influence could be recognized. Fig. 20 shows the % change in failure time of the dam body for % change in K_s value. Negative and positive values in % change in failure time represent respective earlier and delayed computed failure time with changed value of K_s comparison to predicted failure time when K_s value was not changed. The plot shows that increase in K_s value results in rapid increase in moisture movement rate inside the dam body, thereby increasing pore water pressure faster so that failure of the dam takes place earlier. Similarly, decrease in K_s value results in the failure of the dam later.

5. Conclusions

This study conducted a slope-stability analysis using the pore-water pressure and moisture content calculated by a 3D seepage-flow model. Both a conventional water-phase flow model and a water-air two-phase seepage flow model were used for the seepage analysis of a landslide dam. Similarly, in the case of rainfall-induced slope failure, 2D surface flow and an erosion/deposition model were also coupled to the seepage flow models. In most of the cases the numerical simulation results compared well with laboratory experimental measurements in terms of moisture movement, air movement, seepage-outflow rate, surface-water forefront propagation, predicted critical slip surfaces, and time of failure of the considered soil domains. To improve seepage analyses in the unsaturated soil domain, a water-air two-phase flow model has been used to consider the air movement phenomenon inside the domain. The simulated moisture profiles from the water–air two-phase seepage-flow model were delayed slightly compared with those from the one-phase seepage-flow model. Ultimately, the failure time of the slope body and land slide dam were also delayed while considering water–air two-phase seepage-flow. However, the difference in results between the one-phase and two-phase seepage flow considerations were not so much significant. Additionally, the simulated failure time of the model slope and the landslide dam were delayed when using the extended Spencer method for slope-stability analysis compared with Janbu's simplified method of slope-stability analysis. Additional experimental verifications in different soils and field applications are necessary to improve this modeling approach.

Acknowledgements

This research was supported by a grant (11-TI-C06) from Advanced Water Management Research Program funded by Ministry of Land, Infrastructure and Transport of Korean government.

References

Awal, R., Nakagawa, H., Kawaike, K., Baba, Y., and Zhang, H. (2008). "An integrated approach to predict outflow hydrograph due to landslide dam failure by overtopping and sliding." *Annual Journal of Hydraulic Engineering*, JSCE, Vol. 52, pp. 151-156.

Awal, R., Nakagawa, H., Kawaike, K., Baba, Y., and Zhang, H. (2009). "Three dimensional transient seepage and slope stability analysis of landslide dam." *Annuals of Disaster Prevention Research Institute, Kyoto University*, No. 52B, pp. 689-696.

Chen, J., Hopmans, J. W., and Grismer, M. E. (1999). "Parameter estimation of two-fluid capillary pressure-saturation and permeability functions." *Advances in Water Resources*, Vol. 22, No. 5, pp. 479-493.

Crozier, M. J. (1999). "Prediction of rainfall-triggered landslides: A test of the antecedent water status model." *Earth Surface Processes and Landforms*, Vol. 24, No. 9, pp. 825-833.

Dakshanamurthy, V., Fredlund, D. G., and Rahardjo, H. (1984). "Coupled three dimensional consolidation theory of unsaturated porous media." *Proceedings of the Fifth International Conference on Expansive Soils*, Adelaide, South Australia.

Davies, T. R., Manville, V., Kunz, M., and Donadini, L. (2007). "Modeling landslide dambreak flood magnitudes: Case study." *Journal of Hydraulic Engineering*, Vol. 133, No. 7, pp. 713-720.

Fredlund, D. G., Morgenstern, N. R., and Widger, R. A. (1978). "The shear strength of unsaturated soils." *Canadian Geotechnical Journal*, Vol. 15, No. 3, pp. 313-321.

Freeze, R. A. (1978). "Mathematical models of hillslope hydrology." *Hillslope Hydrology*, John Wiley, pp. 177-225.

Fukuzono, T. (1987). "Experimental study of slope failure caused by heavy rainfall." *Erosion and Sedimentation in the Pacific Rim, Proceedings of the Corvallis Symposium*, Oregon, USA.

Jiang, J. C. and Yamagami, T. (2004). "Three-dimensional slope stability analysis using an extended spencer method." *Soils and Foundations, Japanese Geotechnical Society*, Vol. 44, No. 4, pp. 127-135.

Mizuyama, T., Satofuka, Y., Ogawa, K., and Mori, T. (2006). "Estimating the outflow discharge rate from landslide dam outbursts." *Proceedings of the INTERPRAEVENT International Symposium on Disaster Mitigation of Debris Flows,* Slope Failures and Landslides, Vol. 1, No. 2, pp. 365-377.

Mukhlisin, M. and Taha, M. R. (2009). "Slope stability analysis of a weathered granitic hillslope as effects of soil thickness." *European Journal of Scientific Research*, Vol. 30, No. 1, pp. 36-44.

Nakagawa, H. (1989). *Study on risk evaluation of flood and sediment inundation disaster,* PhD Thesis, Kyoto University (in Japanese).

Nakagawa, H., Takahashi, T., Satofuka, Y., and Kawaike, K. (2003). "Numerical simulation of sediment disasters caused by heavy rainfall in Camuri Grande basin." *Proceedings of the Third Conference on Debris-Flow Hazards Mitigation: Mechanics, Prediction,*

and Assessment, Switzerland, Rotterdam, Venezuela 1999, pp. 671-682.

Sassa, K. (1972). "Analysis on slope stability: I, Mainly on the basis of the indoor experiments using the standard sand produced in Toyoura." *Journal of the Japan Society of Erosion Control Engineering,* Vol. 25, No. 2, pp. 5-17 (in Japanese with English abstract).

Sassa, K. (1974). "Analysis on slope stability: II, Mainly on the basis of the indoor experiments using the standard sand produced in Toyoura, Japan." *Journal of the Japan Society of Erosion Control Engineering*, Vol. 26, No. 3, pp. 8-19 (in Japanese with English abstract).

Satofuka, Y., Mori, T., Mizuyama, T., Ogawa, K., and Yoshino, K. (2010). "Prediction of floods caused by landslide dam collapse." *Journal of Disaster Research*, Vol. 5, No. 3, pp. 288-295.

Sharma, R. H. (2006). *Study on integrated modeling of rainfall induced sediment hazards*, PhD Thesis, Kyoto University, Japan.

Takahashi, T. (1991). *Debris flow*, Monograph Series of IAHR, Balkema, pp. 1-165.

Takahashi, T. and Kuang, S. F. (1988). "Hydrograph prediction of debris flow due to failure of landslide dam, Annuals Disaster Prevention Research Institute." *Kyoto Univ.*, No. 31, B-2, pp. 601-615.

Takahashi, T. and Nakagawa, H. (1994). "Flood/debris flow hydrograph due to collapse of natural dam by overtopping." *Journal of Hydroscience and Hydraulic Engineering*, JSCE, Vol. 12, No. 2, pp. 41-49.

Touma, J. and Vauclin, M. (1986). "Experimental and numerical analysis of two-phase infiltration in a partially saturated soil." *Transport in Porous Media*, Vol. 1, No. 1, pp. 27-55.

Tsai, T. L., Chen, H. E., and Yang, J. C. (2008). "Numerical modeling of rainstorm-induced shallow landslides in saturated and unsaturated soils." *Environmental Geology*, Vol. 55, No. 6, pp. 1269-1277.

Tsutsumi, D. and Fujita, M. (2008). "Relative importance of slope material properties and timing of rain fall for the occurance of landslides." *International Journal of Erosion Control Engineering*, Vol. 1, No. 2. pp. 79-89.

Van Genuchten, M. T. (1980). "A closed-form equation for predicting the hydraulic conductivity of unsaturated soils." *Soil Science Society of America Journal*, Vol. 44, No. 5, pp. 892-898.